A CFD and FEM Approach to a Multicompartmental Poroelastic Model for CSF Production and Circulation with Applications in Hydrocephalus Treatment and Cerebral Oedema

John C. VARDAKIS[1], Dean CHOU[1], Brett J. TULLY[2] & Yiannis VENTIKOS[3*]

*Corresponding author: Email: y.ventikos@ucl.ac.uk
1: Institute of Biomedical Engineering and Department of Engineering Science, University of Oxford, Oxford, UK, john.vardakis@eng.ox.ac.uk, dean.chou@eng.ox.ac.uk
2: Oxyntix Ltd., brett.tully@oxyntix.com
3: Department of Mechanical Engineering, University College London, Torrington Place, London, UK.

Abstract This study introduces a Multiple-Network Poroelastic Theory (MPET) model, coupled with finite-volume based Computational fluid dynamics (CFD) for the purpose of studying, in detail, the effects of obstructing Cerebrospinal fluid (CSF) transport within an image-derived cerebral environment. The MPET representation allows the investigation of fluid transport between CSF, brain parenchyma and cerebral blood, in an integral and comprehensive manner. Key novelties of this model are the casting of multidimensional MPET in a Finite Element Method (FEM) framework, the amalgamation of anatomically accurate choroid plexuses with their feeding arteries and a simple relationship relaxing the constraint of a unique permeability for the CSF compartment. This model is used to demonstrate the impact of fourth ventricle outlet obstruction (FVOO). The implications of treating such a clinical condition with the aid of endoscopic third (ETV) and endoscopic fourth (EFV) ventriculostomy are considered. Finally, we outline the impact of the FEM based MPET framework in understanding oedema, and its ongoing evolution.

Keywords: Cerebrospinal Fluid (CSF), Aquaporin-4, Multiple-Network Poroelastic Theory (MPET), Hydrocephalus, Cerebral Oedema

1. Introduction

1.1 Hydrocephalus

Hydrocephalus (HCP) can be succinctly described as the abnormal accumulation (imbalance between production and circulation) of CSF within the brain (Tully, 2011). This balance of CSF production and reabsorption allows the maintenance of the CSF pressure to lie within the approximate range of 600-2000 Pa (Wilson, 2009). HCP cannot be considered a singular pathology, but instead, a consequence of a variety of congenital and acquired disorders present within the CNS (Thompson, 2009). HCP is classified with regards to whether the point of CSF obstruction or discreet lesion lies within the ventricular system (obstructive) and obstructs the flow before it enters the subarachnoid space (Corns, 2012), or not (communicating). It has no known cure and current treatment methods display an unacceptably high failure rate. The two prominent treatment methods – shunt implants and endoscopic third ventriculostomy – are both surgical interventions that are statistically indistinguishable in terms of available clinical survival data and efficacy of short or long term success (Kulkarni, 2010). Ventricular shunting suffers from various complications, high failure rates (up to 50% after two years) and high average costs (Stagno, 2012). There are therefore strong incentives for neurosurgeons to find alternative modes of intervention.

Figure 1 illustrates the ventricular cavity under consideration in this work. In adults, the CSF volume is estimated to be approximately 150 *ml*, where only 25 *ml* are segregated to the ventricles and the remainder occupies the cranial and subarachnoid spaces. When considering adults, the normal CSF circulation proceeds in a consistent and uniform manner since this flow regulation is primarily responsible for cerebral homeostasis (Sakka, 2011). The classical hypothesis of CSF formulation involves the production of CSF at the choroid plexus of the lateral, third and fourth ventricles.

The choroid plexuses possess the added impediment of being the most complicated

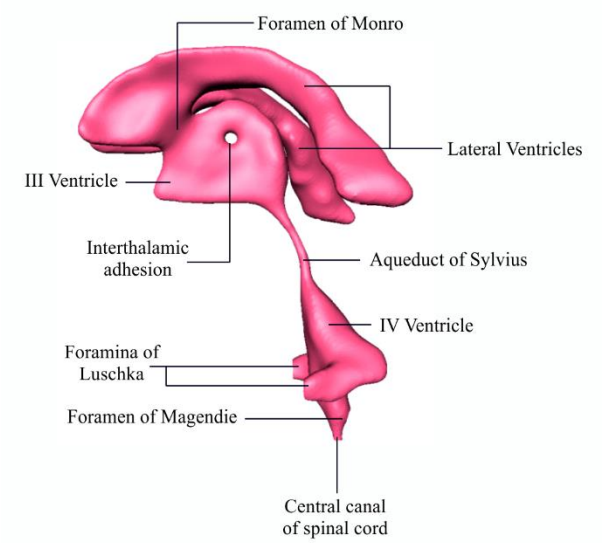

Fig 1. CSF circulates through the four brain ventricles and in the subarachnoid space surrounding the brain and spinal cord.

vascular structures in the brain (Marinkovic, 2005). In this work we also consider the effects of including aquaporin-4 (AQP4) within our mathematical framework. This protein is a water-channel protein expressed strongly in the brain, primarily in astrocyte foot processes at the borders between the brain parenchyma and major fluid compartments. This distribution suggests that AQP4 controls water fluxes into and out of the brain parenchyma. It is the most predominant aquaporin in the brain, and is located on the external and internal glial limiting membranes, the basolateral membrane of ependymal cells (Owler, 2010) and astrocytes. There is a tactical distribution suggesting that AQP4 controls water fluxes into and out of the brain parenchyma. AQP4 is known to possess the essential role of controlling the water balance in the brain and its expression is proving to be pivotal in the regulation and resolution of various forms of oedema (Buffoli, 2010).

Around 600 ml of CSF is produced each day, with a CSF volume replenishment of four (per day) (Irani, 2009). CSF travels from the sites of secretion to the sites of absorption via a unidirectional rostrocaudal flow regime within the cerebral ventricles. It begins to circulate in the cerebroventricular system by flowing out of the lateral ventricles and finally exits through the foramen of Magendie (medial, single) and the bilateral foramina of Luschka. The central canal of the spinal cord also receives CSF from the fourth ventricle; however, in comparison to the foramina of Luschka and foramen of Magendie, this is a minute quantity.

CSF absorption complex. As opposed to the highly orchestrated transport process of CSF secretion, CSF absorption occurs via other outflow mechanisms, such as along the sheaths of major blood vessels and cranial nerves (Abbott, 2004). New functionally intimate links between cerebral interstitial fluid, CSF and extra cranial lymph have been identified (Pollay, 2010). The glymphatic pathway possesses both a lymphatic like system and revolves around AQP4 dependent astroglial water flux which is responsible for the clearance of ISF, CSF and solutes from the parenchyma (Iliff, 2013). Studies have indicated that CSF absorption also occurs along the spinal nerves (Edsbagge, 2004) and across capillary aquaporin channels (Bloch, 2006).

1.2. Oedema

Oedema can be simply described as increased water content in response to brain injury. It is subcategorized into cytotoxic, vasogenic, interstitial or combined. Vasogenic oedema ultimately leads to swelling via an increase in tissue water content, whilst cytotoxic oedema is ultimately characterized by a water compartment shift with no change in tissue water content or volume. Interstitial oedema takes place under the influence of increased intraventricular pressures, and a successful diagnosis of this symptomatic state is possible through the observation of ventriculomegaly and increased periventricular hypodensities (Donkin, 2010; Ho, 2012).

1.3. Endoscopic Third (ETV) and Fourth Ventriculostomy (EFV)

Endoscopic third ventriculostomy (ETV) involved the perforation of the bulging translucent floor of the third ventricle floor (Farin, 2006). This allows for the diversion of the ventricular CSF that has been allowed to build up due to HCP (like Aqueductal stenosis). Similarly to the ETV procedure, EFV involves the perforation of the translucent

membranes blocking the outlets of the fourth ventricle (Fourth Ventricle outlet obstruction (FVOO)), namely the foramen of Magendie and foramina of Luschka (Mohanty, 2008).

2. Multiple-Network Poroelastic Theory (MPET)

The mathematical framework that will be used to interrogate the basic processes that underlie the pathophysiology of HCP along with the more intricate responses (oedema) will now be described. This paper builds upon the work of (Sobey, 2006), (Tully, 2011) and (Vardakis, 2013).

2.1. MPET formulation

In geomechanics and more specifically fractured rock, an MPET medium can be considered as a solid matrix percolated by low porosity pores and high porosity fissures. These pores and fissures are in communication with each other via the transfer of fluid. MPET theory amalgamates porous flow laws, conservation of mass, Terzaghi effective stress and stress-strain relationships. The MPET theory will revolve around the quadruple- MPET model. Biologically, this is derived by accounting for an MPET system that accommodates a high pressure arterial network (*a*), lower pressure arteriole/capillary network (*c*), extracellular/CSF network (*e*) and finally a venous network (*v*). Representing these in a convenient form (Tully, 2011; Vardakis, 2013) in equations (1) to (5) below:

$$\nabla\cdot\boldsymbol{\sigma}-\alpha^a\nabla p^a-\alpha^c\nabla p^c-\alpha^e\nabla p^e-\alpha^v\nabla p^v=0$$

$$\frac{\partial}{\partial t}(c^a p^a+\alpha^a\nabla\cdot\mathbf{u})+\nabla\cdot[-\mathbf{K}^a\cdot\nabla p^a]=\dot{S}_A$$

$$\frac{\partial}{\partial t}(c^c p^c+\alpha^c\nabla\cdot\mathbf{u})+\nabla\cdot[-\mathbf{K}^c\cdot\nabla p^c]=\dot{S}_C$$

$$\frac{\partial}{\partial t}(c^e p^e+\alpha^e\nabla\cdot\mathbf{u})+\nabla\cdot[-\mathbf{K}^e\cdot\nabla p^e]=\dot{S}_E$$

$$\frac{\partial}{\partial t}(c^v p^v+\alpha^v\nabla\cdot\mathbf{u})+\nabla\cdot[-\mathbf{K}^v\cdot\nabla p^c]=\dot{S}_V$$

In equations (1)-(5) above, $\dot{S}_A=-\left|\dot{s}_{a\to c}\right|$, $\dot{S}_C=\left|\dot{s}_{c\to e}\right|-\left|\dot{s}_{e\to v}\right|$, $\dot{S}_E=\left|\dot{s}_{a\to c}\right|-\left|\dot{s}_{c\to e}\right|+\left|\dot{s}_{c\to v}\right|$,

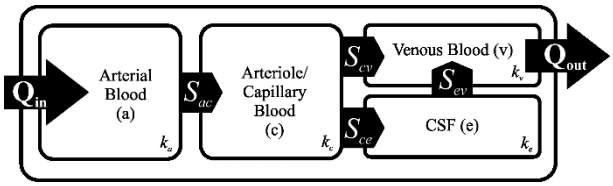

Fig 2. The above schematic represents the transfer restrictions placed on the MPET model. For example, it can be seen that flow is prohibited between the CSF and arterial network.

$\dot{S}_V=\left|\dot{s}_{e\to v}\right|+\left|\dot{s}_{c\to v}\right|$, $c^\phi(>0)=1/Q^\phi$ is a storage coefficient, where $\phi=[a,e,c,v]$ and Q^ϕ is deemed as the amalgamated compressibility of both fluid and solid phases (it is related to the bulk moduli) at the relevant compartment, $\dot{s}_{b\to a}$ are source or sink terms which arise from the rate of fluid transfer between networks $b\to a$ (network transfer coefficients) and:

$$\boldsymbol{\sigma}=\lambda\,\mathrm{tr}(\boldsymbol{e})+2\tilde{\mu}\boldsymbol{e}-\alpha p\mathbf{I} \tag{6}$$

$$\boldsymbol{e}(\mathbf{u})=\frac{1}{2}(\nabla\mathbf{u}+\nabla\mathbf{u}^T) \tag{7}$$

In the above constitutive equations, $\mathbf{u}(\mathbf{x},t)$ is the displacement of the porous medium (describes the mean displacement of particles forming the solid matrix), $\mathbf{p}^\phi(\mathbf{x},t)$ is the fluid pressure of each compartment, $\boldsymbol{\sigma}(\mathbf{x},t)$ is the total stress tensor, $\mathbf{K}^\phi(\mathbf{x})$ is a symmetric and uniformly positive definite tensor representing the permeability (isotropic) divided the fluid viscosity at each compartment (κ^ϕ/μ^ϕ) , α^ϕ is the Biot-Willis constant for each compartment and λ and $\tilde{\mu}$ are the Lamé constants.

The MPET system is completed with the following boundary conditions for each of the four compartments (Arterial, Arteriole/Capillary blood, Venous blood and CSF), in which Γ_S and Γ_V are boundary conditions at the skull and ventricles respectively (8.1 – 8.12 below):

$$\mathbf{u}=0 \quad \text{on} \quad \Gamma_S \ ,$$

$$-p_V\mathbf{n}=\sigma\cdot\mathbf{t}_\mathbf{N} \quad \text{on} \quad \Gamma_V \ ,$$

$$p^a|_{\Gamma_S}=p_{bpA} \quad \text{on} \quad \Gamma_S \ ,$$

$$p^a\cdot\mathbf{n}|_{\Gamma_V}=0 \quad \text{on} \quad \Gamma_V \ ,$$

$$p^c\cdot\mathbf{n}|_{\Gamma_S}=0 \quad \text{on} \quad \Gamma_S \ ,$$

$$p^c \cdot \mathbf{n}|_{\Gamma_V} = \frac{Q_p}{\kappa_{c-vent}} \quad \text{on} \quad \Gamma_V,$$

$$p^v \cdot \mathbf{n}|_{\Gamma_S} = p_{bp} \quad \text{on} \quad \Gamma_S,$$

$$p^v \cdot \mathbf{n}|_{\Gamma_V} = 0 \quad \text{on} \quad \Gamma_V,$$

$$p_S^e|_{\Gamma_S} = p^v|_{\Gamma_S} + \mu^e R Q_o \quad \text{on} \quad \Gamma_S,$$

$$p_S^e|_{\Gamma_S} = p_{bp} + \mu^e R Q_o \quad \text{on} \quad \Gamma_S,$$

$$\frac{p_S^e - p_{bp}}{\mu^e R} = \frac{\pi d^4}{128 \mu^e L}(p_V^e - p_S^e) + \oint_S (-\mathbf{K}^e \cdot \nabla p^e) \cdot \mathbf{n} ds \quad \text{on} \quad \Gamma_S$$

$$\dot{V} = Q_p - \frac{\pi d^4}{128 \mu^e L}(p_V^e - p_S^e) - S(p_V|_{\Gamma_V}) - \oint_V (-\mathbf{K}^e \cdot \nabla p^e) \cdot \mathbf{n} ds \quad \text{on} \quad \Gamma_V$$

This is an adult brain that is being taken under consideration; hence a rigid wall approximation can be envisaged stemming from the elimination of layers like the dura mater and scalp. CSF is assumed to be produced at a constant rate, Q_p within the ventricles. p_{bp} and p_{bpA} are the arterial blood pressure and blood pressure in the sagittal sinus respectively, κ_{c-vent} represents the capillary network resistance to the flow from the capillary network $\left(\kappa_{c-vent} = 6 \times 10^{-4}\, m^5 s/kg\right)$, R is the resistance due to arachnoid granulations and finally Q_o is the efflux of CSF at the region of the skull. It is necessary to restrict the transfer of water between fluid networks, and Figure 2 sketches the setting in which the quadruple MPET model functions. The transfer between networks is via a hydrostatic pressure gradient, where s_{st} is a constant scaling the flow between networks *s* and *t*. The parameter(s) $\dot{s}$ denote network transfer coefficients.

2.3 1D MPET Coupling with CFD

Assuming a linear stress-strain relationship and isotropic permeability, then the effective stress is represented by Hooke's law, and is inverted for stress and subsequently represented as a function of displacement with the aid of Einstein notation to calculate divergence:

$$\nabla \cdot \boldsymbol{\sigma} = G \nabla^2 \mathbf{u} + \frac{G}{1-2\nu} \nabla\left(\nabla \cdot \mathbf{u}\right) \qquad (9)$$

From the above, *G* is the shear modulus and is equivalent to $G = E(1-2\nu)^{-1}$, where *E* is the Young's modulus and *v* is the Poisson ratio.

An isotropic permeability would imply $k_{ij} = k\delta_{ij} = \left(\kappa\mu^{-1}\right)\delta_{ij}$. The final system of equations utilises a one-dimensional, spherically symmetric geometrical representation, which is provided by the transformation of the nabla operator in spherical coordinates. In the context of the biological system under consideration, the following assumptions are also made to simplify the nabla transformation: $x = [r, \theta, \varphi]$, $u = [u(r), 0, 0]$ and $p = p(r)$.

The parenchyma of an adult brain is represented as a spherical shell. The outer radius of this shell is given by r_M, whilst the lumped representation of the lateral ventricles are represented by another spherical shell with radius. The third and fourth ventricles along with the Sylvian aqueduct are assumed to be connected to the subarachnoid space (SAS). The parameters: μ_A, κ_A, α_A, where A = [a,e,c,v], represent the viscosity, permeability and Biot parameters of the interstitial fluid networks. The geometry representing all the features of the ventricles arise from a volunteer scan outlined in §2.7. Additional assumptions include the notion that HCP has a long time scale for development, of the order of days, weeks or even years (if one considers the chronic case). It is therefore evident that an assumption of a quasi-steady system is not unrealistic. In the 1D MPET - CFD coupling, we do not take pulsatile effects into account. This new quasi-steady constraint, $\partial^2/\partial t^2$ and $\partial/\partial t \to 0$. When executing the CFD simulations to determine the CSF flow dynamics through the ventricular system, the flux of CSF exiting the outlets is used to replace the Poiseuille assumption in equation 8.11 and 8.12.

2.4 1D MPET-CFD Implementation

The governing multicompartmental poroelastic equations are solved with an implicit second-order central finite differences scheme on the midpoints and forward/backward Euler used

on the boundary nodes. The quasi-steady time discretization (for the temporally dependent terms in the boundary conditions) is performed via a first-order Euler approach. Flow through the multidimensional aqueducts is solved using the multiphysics software CFD-ACE+ (ESI Group, Paris France), along with central spatial differencing, algebraic multigrid scheme and the SIMPLEC pressure–velocity coupling. The coupling between the poroelastic solver and the flow solver is achieved through appropriate CFD-ACE+ user-defined subroutines.

Mesh generation for the 3D volumes was achieved via the use of CFD-VisCART (ESI Group, Paris France), which is an unstructured adaptive Cartesian grid generation system. For the entire system, over 2 million cells were used for each simulated case. Grid independence analysis has shown that this resolution is adequate for the problem at hand.

2.5 The 2D Finite Element Formulation

In this section, we outline how the MPET equations (1-5) and the associated boundary conditions (8) are solved using a finite element scheme in two dimensions, as opposed to the 1D MPET-CFD coupling in §2.3.

Let $\Omega \subset \mathbb{R}^2$ be a domain with Lipschitz continuous boundary $\partial\Omega$ and unit outward normal **n**. The triangulation T of Ω is a set $\{T\}$ of triangles *T*, where $\Omega = \cup_{T\in \mathrm{T}} T$. The intersection of two triangles is either an edge, empty or a corner. The mesh does not contain any hanging nodes. The family of triangular partitions is assumed to be shape-regular and quasi-uniform in order to optimally approximate the finite element space in the MPET system already outlined. We subsequently arm the polynomial functional space $\wp$ on T with shape functions for the linear and quadratic Lagrange triangles.

The linear and quadratic Lagrange triangles possess canonical bases of $\{1, r, s\}$ and $\{1, r, s, r^2, rs, s^2\}$ respectively. Finally, we isoparametrically map the triangular elements in the manner $(x, y) \mapsto (r, s)$. For the FEM formulation, we relax spherical symmetry and the quasi-steady approximation and refrain from making use of equation 9.

We spatially discretize our system through the weak form of the liquid and solid phases via the multiplication of relevant test functions and integrating by parts, and finally apply our boundary conditions (8.1-8.12). The time integration is obtained via a spatial-semi discretization of the liquid phases where the space discreet solution $p_h^A(t)$ is obtained for each compartment via the solution of the system of ODE's which satisfy $\xi_i(t)$ (time-dependent nodal values). Here, we employ the implicit backward-Euler method.

2.6 AQP4 swelling characteristics and non-linear permeability

In the 1D-CFD coupling, the following relationship was proposed to alleviate the constraint of a unique permeability for the CSF compartment in order to account for AQP4's swelling characteristics:

$$k_i = \left(k_e / \mu_e\right)\left[1 - \left(\frac{P_e - P_{ref}}{P_{ref}}\right)\right](A_f) \tag{10}$$

From equation 10, k_e and μ_e have already been described, P_e is the CSF pressure, P_{ref} is a reference pressure and finally A_f is an amplification factor, and here it has a value of unity. The permeability was made to vary between the interval $1.4\cdot10^{-14} \le k_e \le 9.9\cdot10^{-14}$, and coupled with the varying CSF pressure P_e. P_{ref} was chosen to possess a value $P_{ref} = 1\ kPa$. Due to insufficient experimental data, AQP4 expression is not accounted for in equation 10. For the FE formulation, we appreciate that since a volume reduction leads to a smaller pore size and consequently a lower permeability, the CSF/ISF compartment is augmented to include a non-linear permeability, namely in the form:

$$\frac{\partial}{\partial t}(c^e p^e + \alpha^e \nabla\cdot\mathbf{u}) = \nabla\cdot[\hbar_{csf}\cdot\nabla p^e] + \dot{S}_e \tag{11}$$

where $\hbar_{csf} = \mathbf{K}_e\, \mathrm{e}^{M(\epsilon)}$. Here, the constant *M* is initially given as 4.3 (Sobey, 2006). In the above equation, $\dot{S}_e = \dot{s}_{c\to e} - \dot{s}_{v\to e}$ and $\boldsymbol{\epsilon} = \nabla\cdot\mathbf{u}$. The Lax-Milgram lemma is satisfied by

using $\hbar_{csf}(u)$. In order to account for the non-linear nature of the permeability, we apply a Newton-Galerkin Method formulation for the aforementioned compartment within the MPET framework.

Finally, we define a useful parameter, namely the increment of fluid content, ζ, in terms of strain, ε as:

$$\zeta = \alpha\varepsilon + \frac{(1-\alpha\beta)\alpha}{K\beta}\, p \qquad (12)$$

In equation 12, ε is the dilation, β is Skempton's coefficient (β = 0.99 throughout the MPET framework) and *K*, the bulk modulus, is given by $K = \lambda + 2G/3$, where λ and G have values of 524 Pa and 216 Pa respectively. β essentially denotes the measure the distribution of the applied stress between the solid matrix and CSF. A value of β = 0.99 represents a saturated mixture where the applied load is nearly entirely supported by the CSF fluid. The values of all other constants used can be found in (Tully, 2011; Vardakis, 2013).

2.7 Model Implementation

The 2D FEM based MPET system is implemented in the MATLAB (R2013a) environment. This includes the geometry preparation and mesh generation.

2.8 Anatomy acquisition

Imaging was performed on a 1.5T GE Signa system (Waukesha, WI, USA) and a T2 weighted imaging sequence was used for obtaining the brain anatomy data of a male volunteer. Images were acquired axially covering the whole brain at a voxel size of 1×0.5×2 mm^3. The acquired voxels were manually segmented for the ventricular system using Amira (Mercury Computer Systems, San Diego, CA, USA) and the raw segmented geometry from this process was converted to a Stereo Lithography (STL) file. In order to preserve key anatomical features smoothing of the STL file was done using the open-source modelling software, Blender (The Blender Foundation).

3. Results & Discussion

3.1 IVth Ventricular Outlet Obstruction (CFD)

In this work, obstructive HCP was investigated via the occlusion of individual or a combination of outlets of the fourth ventricle. The physical comparators used to describe the effects of this induced HCP include ventricular displacement, CSF pressure, peak velocities, pressure difference between lateral and fourth ventricle and wall shear stress. These comparators are also used to give an indication of the alleviating effects of the two surgical procedures proposed. From the results garnered in this study we observe that the central canal does not simply act as a pathway for CSF flow. Gupta and colleagues speculate that very little fluid passes through this ventricular boundary (Gupta, 2009), and indeed this may seem to be the case under typical aqueductal stenosis.

During the cases of FVOO, where the peak velocity in the central canal exceeded 35 cm/s during the combined occlusion of the bilateral foramina and the foramen of Magendie, the application of both ETV and EFV reduced the impact of the occlusions on the central canal for nearly all cases; however, ETV did so with greater success, as can be seen from the results in Table 1. The ventricular displacement was noted to increase with increasing severity of aqueductal stenosis, up to a maximum of 3.28 mm. Applying ETV at the floor of the third ventricle reduces both the ventricular displacement and CSF compartmental pressure to manageable levels.

FVOO (site)	v_p [cm/s]	ΔP [Pa]	WSS [N/m^2]
Luschka (Lu)	16.5/8.9/●/8.7	17	0.83
Magendie (Ma)	16.6/●/2.9/2.6	17	0.82
Lu + Ma	15/●/●/35.5	16	0.63
Lu + ETV	8.9/4.2/●/3.9	< 10	0.29
Ma + ETV	9/●/1.4/1.1	< 10	0.33
Lu + Ma + ETV	8.5/●/●/5.6	< 10	0.31
Lu + EFV	16.2/3/●/2.6	17	0.79
Ma + EFV	16.2/●/1.7/1.3	17	0.79
Lu + Ma + EFV	17/●/●/4.6	18	0.86

Table 1. The values of peak velocity v_p (in the aqueduct (a), Magendie (m), Luschka (l, average) and central canal (cc)), pressure difference between isolated points in the lateral ventricle and fourth ventricle, ΔP and wall shear stress (WSS) are given for the occluded foramina of Luschka and foramen of Magendie. The peak velocity values for endoscopic third and fourth ventriculostomy (ETV, EFV) are also displayed. There a four separate values for peak velocity, v_p. From left to right these are: aqueductal, Magendie, Luschka (average) and central canal. ● indicates full occlusion. All values obtained at t = 50s.

We also observed that the aqueduct tries to maintain the laminar CSF flow ($350 < Re < 700$) through the third and fourth ventricle by assisting in repelling the core of central fluid from the aqueductal wall effects, a pressure gradient develops to help maintain this flow of CSF (rising from around 18 Pa to 241 Pa when considering aqueductal stenosis.

During atresia (by translucent membranes) of the bilateral foramina or foramen of Magendie, the pressure difference between the lateral ventricle cavity and the fourth ventricle remains at approximately 17 Pa. The effect that atresia of the fourth ventricular exits has on the CSF flow within the ventricular system is questionable. Provided that not all of the exits of the fourth ventricle are blocked (i.e. the central canal remains open), the peak aqueductal velocity would decrease by a relatively modest amount (15.0 cm/s), as in the case of the tri-exit closure (bilateral foramina and foramen of Magendie). The bulk flow increase would directly be associated with the central canal, as in the simulated case. The peak aqueductal velocity increased substantially to 35.5 cm/s.

One could appreciate that such a form of pronounced atresia could initiate secondary pathologies to FVOO, such as Syringomyelia. Recent developments indicate an increase in the expression of AQP4 in combination with the level of central canal occlusion and subsequent dilation (Zhang, 2012). Once the atresia is perforated during EFV, a largely reduced and constant aqueductal peak velocity is recorded. This is a moderate increase from that witnessed for the patent aqueduct. The central canal is alleviated from the burden of having to displace most of the CSF egress. Ventricular displacement is reduced to the same level for all cases of atresia during application of EFV, whilst the CSF pressure is elevated back to a similar level seen in the case of a healthy individual. What was interesting is that although the management of the FVOO seems to be commensurate, it must be noted that ETV performed better in comparison, reducing: the average peak velocity in the aqueduct for the three cases of atresia, the pressure difference ΔP was reduced further, wall shear stress as well as ventricular displacement. CSF pressure was reduced below the levels expected from an individual with an open aqueduct. This fortifies the view of Mohanty and colleagues that stipulate ETV should be the preferred treatment for FVOO (Mohanty, 2008). EFV can be deemed as a viable alternative, especially when cases such as the one described by Gianetti (Gianetti, 2011), where the foramen of Monro and third ventricle did not satisfy prerequisite size constraints for suitable ETV adaptation.

The unique permeability of the CSF compartment (k_e) was relaxed in this study, and given way to a fluctuating adaptation represented by equation 10. The reference pressure was arbitrarily chosen to have a value of 1 kPa. If CSF pressure $P_e < P_{ref}$, then the permeability increases, whilst the converse is true for $P_e > P_{ref}$. The aim of this varying permeability compartment was to bring to light a very simple feedback mechanism that would theoretically counteract the effects of ventricular dilation and subsequent elevations of CSF pressure through the efflux of excess CSF to the blood system (Tait, 2008).

3.2 MPET-FEM formulation

In Figure 3, all velocity values are negative for the capillary compartment of the MPET system. In the CSF compartment, values as high as 6×10^{-4} are witnessed for the fluid increment close to the ventricles, with subsequent compression against the rigid skull in the surrounding parenchyma.

It was observed that fluid content in general increased in areas of high convexity such as

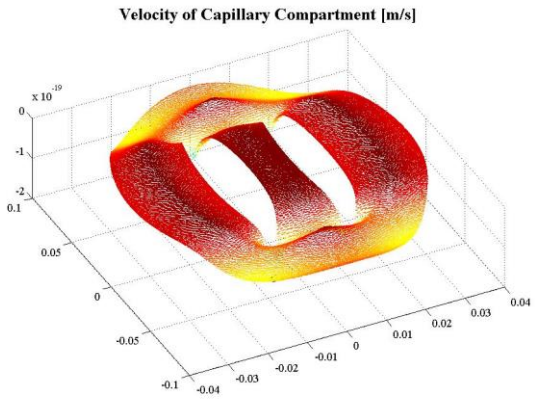

Fig 3. The above MPET-FEM simulation shows the distribution of fluid velocity in the capillary compartment. Taken at *t=50s.*

the ventricle walls since tissue near the ventricular regions is stretched to such an extent (during ventricular enlargement) that there is an overall increase in porous space and hence fluid content. The in-house FEM-MPET formulation allows us to investigate a plethora of aspects relating to the solid and fluid phases both individually and as a unified system.

The code allows us to investigate the structural mechanics aspects of our 2D elastic FEM solver, specifically for the solid phase, whilst embedding this system within a communicating system of liquid phases.

Current studies also investigate the effect of boundary conditions and source/sink terms of the liquid phases. The non-linear treatment of the deformation dependent permeability using a Newton-Galerkin approach provides promising results in the understanding of interstitial oedema. In the results shown in Fig 3, we represent the skull and ventricles as ellipses of anatomically appropriate axes, however, the 2D MPET-FEM formulation allows for the incorporation of anatomically accurate representations of cerebral slices. The current 2D MPET-FEM system is also extendable to three dimensions, where we base the formulation on tetrahedral elements. We also bring to light a 3D discontinuous Galerkin (dG) MPET framework. It is a versatile system with n^{th} order shape function functionality for the tetrahedral elements which can also take warping into account.

4. Acknowledgments

This work is financially supported by the Digital Economy Programme. VPH-DARE@IT is also kindly acknowledged. The EPSRC is further acknowledged for providing the resources necessary for the High Performance Computing simulations conducted in this study, through grant EP/F033710/1. Finally, the ESI Group and Dr. M. Megahed are kindly acknowledged for allowing the use of the CFD-ACE+ multiphysics suite.

5. References

Tully, B., & Ventikos, Y. (2011). Cerebral water transport using multiple-network poroelastic theory: application to normal pressure hydrocephalus. *Journal of Fluid Mechanics, 667*, 188-215.

Wilson, R., & Williams, M. (2009). Disorders of intracranial pressure and cerebrospinal fluid circulation. In D. Irani (Ed.), *Cerebrospinal Fluid in Clinical Practice* (pp. 99-104). Philadelphia: Saunders Elsevier.

Thompson, D. (2009). Hydrocephalus. *Neurosurgery*, 130-134.

Corns, R., & Martin, A. (2012). Hydrocephalus. *Neurosurgery, 30*(3), 142-148.

Kulkarni, A. V., Drake, J. M., Kestle, J. R. W., Mallucci, C. L., Sgouros, S., & Constantini, S. (2010). Endoscopic Third Ventriculostomy Vs Cerebrospinal Fluid Shunt in the Treatment of Hydrocephalus in Children: A Propensity Score - Adjusted Analysis. *Neurosurgery, 67*, 588-593.

Stagno, V., Navarette, E. A., Mirone, G., & Esposito, F. (2012). Management of Hydrocephalus Around the World. *World Neurosurgery*.

Sakka, L., Coll, G., & Chazal, J. (2011). Anatomy and physiology of cerebrospinal fluid. *European Annals of Otorhinolaryngology, 128*, 309-316.

Marinkovic, S., Gibo, H., Milisavljevic, M., Djulejic, V., & Jovanovic, V. (2005). Microanatomy of the Intrachoroidal Vasculature of the Lateral Ventricle. *Operative Neurosurgery, 57*(1), 22-36.

Owler B, Pitham T, Wang D. (2010) Aquaporins: relevance to cerebrospinal fluid physiology and therapeutic potential in hydrocephalus. *Cerebrospinal Fluid Research, 7*, 1–12.

Buffoli, B. (2010). Aquaporin biology and nervous system. *Current Neuropharmacology, 8*, 97-104.

Irani, D. (2009). *Cerebrospinal Fluid in Clinical Practice*. Philadelphia, PA, USA: Saunders Elsevier.

Abbott, J. N. (2004). Evidence for bulk flow of brain interstitial fluid: significance for physiology and pathology. *Neurochemistry International, 45*, 545-552.

Pollay, M. (2010). The function and structure of the cerebrospinal fluid outflow system. *Cerebrospinal Fluid Research, 7*(9), 1-20.

Iliff, J. J., Wang, M., Liao, Y., Plogg, B. A., Peng, W., Gundersen, G. A., . . . Nedergaard, M. (2012). A Paravascular Pathway Facilitates CSF Flow Through the Brain Parenchyma and the Clearance of Interstitial Solutes, Including Amyloid β. *Sci Transl Med, 4*(147), 1-11.

Edsbagge, M., Tsell, M., Jacobsson, L., & Wikkelso, C. (2004). Spinal CSF absorption in healthy individuals. *American Journal Physiology Reguationl Integrative Computational Physiology, 287*, 1450-1455.

Ho, M., Rojas, R., Eisenberg, R.L. (2012). Cerebral Edema. *American Journal of Roentgenology, 199*, W258-W273.

Donkin, J. J.; Vink, R., Mechanisms of cerebral edema in traumatic brain injury: therapeutic developments. *Current Opinion in Neurology, 23*(3), 293-299.

Bloch, O., Auguste, K., Manley , G., & Verkman , A. (2006). Accelerated progression of kaolin-induced hydrocephalus in aquaporin-4 deficient mice. *Cerebral Blood Flow Metabolism, 26*, 1527-1537.

Farin, A., Aryan, H. E., Ozgur, B., Parsa, A., & Levy, M. (2005). Endoscopic Third Ventriculostomy. *1*(13).

Mohanty, A., Biswas, A., Satish, S., & Vollmer, D. G. (2008). Efficacy of Endoscopic Third Ventriculostomy in Fourth Ventricular Outlet Obstruction. *Neurosurgery, 63*(5), 905-914.

Vardakis, J. C., Tully, B. J., & Ventikos, Y. (2013). Multicompartmental poroelasticity as a platform for the integrative modelling of water transport in the brain. In G. A. Holzapfel & E. Kuhl (Eds.), *Computer Models in Biomechanics: from Nano to Macro* (pp. 305-316). Heidelberg: Springer-Verlag.

Vardakis J. C., Tully B. J., Ventikos Y. (2013) Exploring the Efficacy of Endoscopic Ventriculostomy for Hydrocephalus Treatment via a Multicompartmental Poroelastic Model of CSF Transport: A Computational Perspective. *PLoS ONE*, 8(12): e84577.

Sobey, I., & Wirth, B. (2006). Effect of non-linear permeability in a spherically symmetric model of hydrocephalus. *Mathematical Medicine and Biology, 23*, 339-361.

Gupta, S., Soellinger, M., Boesiger, P., Poulikakos, D., & Kurtcuoglu, V. (2009). Three-Dimensional Computational Modeling of Subject-Specific Cerebrospinal Fluid Flow in the Subarachnoid Space. *Biomechanical Engineering, 131*.

Gianetti, A., Malheiros, A., & Silva, M. (2011). Fourth ventriculostomy: an alternative treatment for hydrocephalus due to atresia of the Magendie and Luschka foramina. *Neurosurgical Pediatrics, 7*, 152-156.

Tait, M. J., Saadoun, S., Bell, B. A., & Papadopoulos, M. C. (2008). Water movements in the brain: role of aquaporins. *TRENDS in Neurosciences, 31*(1), 37-43.

Zhang, Y., Ping Zhang, Y., Shields, L., Zheng, Y., Xu, X.-M., Whittemore, S. R., & Shields, C. (2012). Cervical Central Canal Occlusion Induces Noncommunicating Syringomyelia. *Neurosurgery*.